Chemical Science

EDGE ARTICLE

View Article Online
View Journal | View Issue

Check for updates

Cite this: *Chem. Sci.*, 2025, **16**, 19244

All publication charges for this article have been paid for by the Royal Society of Chemistry

Multi-level macrocyclic assembly achieving organic upconversion delayed fluorescence for targeted cell imaging

Jie Niu,†[b] Xuan Wu,†[c] Jie Yu,[a] Zhuo Lei,[a] Ying-Ming Zhang,*[a] Li-Hua Wang,[a] Jing Wu,[d] Jie Han *[c] and Yu Liu *[a]

Purely organic room-temperature phosphorescence (PORTP) supramolecular materials have been widely explored in bioimaging, but their relatively short excitation wavelengths limit their further application. Herein, we report a purely organic phosphorescence resonance energy transfer (PRET) assembly, which was constructed by purely organic upconversion phosphor 6-bromoisoquinolium-modified permethylated β-cyclodextrin (BQ-PCD), cucurbit[8]uril (CB[8]) and tetra(4-sulfonatophenyl)porphyrin (TPPS), displaying not only CB[8]-confinement enhanced PORTP, but also multi-photon-mediated PRET achieving delayed deep-red luminescence for targeted cell imaging. Compared with BQ-PCD, the BQ-PCD⊂CB[8] supramolecular assembly remarkably prolongs PORTP lifetime from 13.8 ns to 640 μs, and further assembles with TPPS through strong host–guest interaction between PCD and TPPS, achieving delayed deep-red luminescence with a lifetime of around 11 μs through a highly efficient PRET process (94.5%). Taking advantage of the 1 : 2 stoichiometric ratio, BQ-PCD⊂CB[8] efficiently enhanced the upconversion process compared with BQ-PCD⊂CB[7], leading to delayed deep-red luminescence under multi-photon excitation at 920 nm in TPPS⊂BQ-PCD⊂CB[8]. With the further cascade assembly with tumor-targeting hyaluronic acid (HA), the upconversion supramolecular nanoparticle could be successfully applied for targeted cell imaging through an upconversion PRET process. This study offers a novel approach to fabricating long-lived deep-red fluorescence materials with upconversion properties *via* macrocyclic confinement assembly.

Received 16th July 2025
Accepted 2nd September 2025

DOI: 10.1039/d5sc05297a

rsc.li/chemical-science

Introduction

In recent years, purely organic room-temperature phosphorescence (PORTP) materials[1–4] have attracted significant attention due to their long triplet lifetime and large Stokes shift, making them highly promising for applications in biological imaging,[5,6] sensing,[7,8] anti-counterfeiting,[9–11] and electrochemical devices.[12–14] In particular, RTP materials with deep-red or near-infrared (NIR) emission features have been widely explored in time-resolved imaging and chemo/biosensing, due to their intrinsic advantages of excellent spatial resolution, deep tissue penetration, and minimal background interference.[15–19] However, most RTP materials have relatively short excitation wavelengths in the UV light region (<400 nm),[20,21] which limits their broader application in bio-imaging. Therefore, there is growing interest in developing RTP materials that can be excited by NIR light, which could reduce potential safety concerns and enhance tissue penetration for biomedical applications. To overcome such shortcomings, upconversion technology has been considered as a promising approach, in which the long excitation wavelength with low energy could be converted to high energy emission with a relatively short wavelength.[22,23] Therefore, tremendous efforts have been focused on the fabrication of long-lived deep-red or NIR materials by the incorporation of inorganic upconversion nanoparticles.[24] For example, we reported the macrocyclic confinement of bromophenylpyridinium-modified HA supramolecular RTP materials, which could also be realized under NIR excitation by incorporating inorganic rare earth upconversion nanoparticles.[25] However, the realization of upconversion RTP materials in purely organic systems remains challenging, especially within one organic compound containing both RTP and upconversion properties.

It is well known that macrocyclic confinement assembly has been widely employed to fabricate efficient RTP materials in an aqueous solution, which could provide hydrophobic and rigid

---

[a] *College of Chemistry, State Key Laboratory of Elemento-Organic Chemistry, Nankai University, Tianjin 300071, P. R. China. E-mail: ymzhang@nankai.edu.cn; yuliu@nankai.edu.cn*

[b] *Medical College, Department of Basic Medicine and Medical Technology, Yangzhou University, Yangzhou, Jiangsu 225009, China*

[c] *School of Chemistry and Chemical Engineering, Yangzhou University, Yangzhou, Jiangsu 225002, P. R. China. E-mail: hanjie@yzu.edu.cn*

[d] *Biological Imaging and Analysis Laboratory, Medical and Health Analysis Center, Peking University, Beijing 100191, P. R. China*

† These authors contributed equally to this work.

cavities to encapsulate the phosphors with high binding constants, shielding them from water and oxygen molecules, suppressing non-radiative transitions, and improving the intersystem crossing efficiency.[26] Among all macrocycles, cucurbit[8]uril (CB[8]) exhibits a unique ability to encapsulate two guest molecules simultaneously, forming a stable 1 : 2 host–guest complex by promoting intermolecular charge–transfer interactions,[27,28] which could not only enhance phosphorescence properties[29] but also achieve multi-photon absorption properties.[30] Moreover, macrocyclic confinement assembly could also result in a highly efficient phosphorescence resonance energy transfer (PRET) process by the cascade encapsulation of different luminescent groups, especially in multi-macrocyclic confinement assembly systems. In these systems, different functional groups would be encapsulated into respective cavities, not only promoting their luminescence performance, but also reducing the distance between phosphorescent donors and fluorescent acceptors.[31] Along these lines, some macrocyclic confinement assemblies have been successfully constructed by incorporating commercially available fluorescent dyes to achieve long-lived luminescence emission in the deep-red or NIR region for cell imaging, anti-counterfeiting, and biosensing.[32–34] However, to the best of our knowledge, the construction of PORTP materials by using single molecule organic compounds with both phosphorescence performance and upconversion ability to achieve delayed deep-red luminescence with high PRET efficiency for targeted cell imaging has rarely been reported.

Herein, we wish to report an upconversion PORTP supramolecular assembly, in which the 6-bromoisoquinolium-modified permethylated β-cyclodextrin (BQ-PCD) is the phosphor with upconversion ability, cucurbit[8]uril (CB[8]) could enhance both the RTP and upconversion performance of BQ-PCD through the macrocyclic confinement effect, and PCD would link the phosphorescence donor (BQ motif) and fluorescence acceptor (tetra(4-sulfonatophenyl)porphyrin, TPPS) through strong host–guest interactions, which is successfully applied for targeted delayed deep-red cell imaging with excitation at 920 nm. In the BQ-PCD, designed as a phosphor possessing dual host–guest binding sites, the BQ moiety could be firstly encapsulated by CB[8] in a 2 : 1 stoichiometric ratio, leading to PORTP emission at 530 nm with a prolonged lifetime of 684.0 μs. Furthermore, this BQ-PCD⊂CB[8] complex also exhibits an enhanced multi-photon absorption ability compared with BQ-PCD and BQ-PCD⊂CB[7], in which the PORTP at 530 nm could also be achieved under three-photon excitation at 920 nm. Meanwhile, the PCD cavity in BQ-PCD⊂CB[8] would bind TPPS with a high binding constant up to 10^{12} M^{-2}, resulting in delayed deep-red luminescence at 645 nm and 710 nm with a high PRET efficiency of 94.5%, and this PRET process could also be realized under 920 nm irradiation. Furthermore, after co-assembly with tumor-targeting hyaluronic acid (HA), efficient upconversion PRET was achieved with the HA/TPPS⊂BQ-PCD⊂CB[8] system for targeted delayed fluorescence (DF) imaging of cancer cells. This study presents a novel multi-photon absorption approach to achieving highly efficient PRET for delayed fluorescence imaging based on macrocyclic confinement assembly (Scheme 1).

Results and discussion

Synthesis and structural characterization

The phosphor 6-bromoisoquinolium modified permethylated β-cyclodextrin (BQ-PCD) was synthesized *via* a "click" reaction according to the reported method,[35] and characterized through ^{1}H NMR and high-resolution mass spectrometry (HRMS) (Fig. S1 and S2, SI). 2D ROESY spectroscopy was employed to

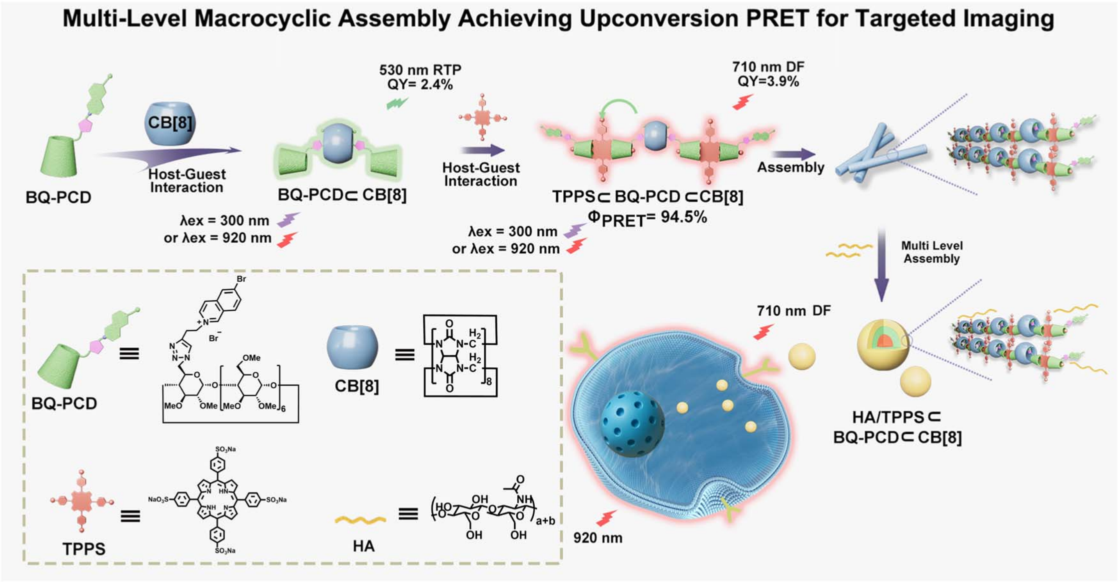

Scheme 1 Schematic illustration of multi-level macrocyclic assembly achieving organic upconversion PRET for targeted delayed fluorescence cell imaging.

further illustrate the molecular binding model of BQ-PCD (Fig. S3, SI), which indicated no self-inclusion or exclusion structure could be formed by BQ-PCD itself.

Binding behaviour of CB[8] and BQ-PCD

Due to the existence of 6-bromoisoquinolium (BQ) and per-methylated cyclodextrin (PCD) motifs, the BQ-PCD could act as the guest molecule for CB[8], as well as host molecule for TPPS. First, the host–guest complexation between CB[8] and BQ-PCD was studied by NMR spectroscopy. From the obtained ^{1}H NMR spectra (Fig. 1a), the peaks at 9.57, 8.55, 8.52, 8.36, 8.26, and 8.19 ppm were assigned to the H_c, H_d, H_f, H_e, H_a, and H_b protons of the BQ motif in BQ-PCD, and the peak at 7.93 ppm was assigned to H_g on the triazole motif. After the addition of CB[8], the H_c signal shifted to 9.49 ppm ($\Delta\delta = -0.08$ ppm), H_d shifted to 7.09 ppm ($\Delta\delta = -1.46$ ppm), H_f shifted to 8.21 ppm ($\Delta\delta = -0.31$ ppm), H_e shifted to 7.96 ppm ($\Delta\delta = -0.40$ ppm), H_a shifted to 7.17 ppm ($\Delta\delta = -1.09$ ppm), and H_b shifted to 6.42 ppm ($\Delta\delta = -1.72$ ppm). The proton signals assigned to H_{a-f} in 6-bromoisoquinolium shifted upfield upon the addition of CB[8] into the BQ-PCD solution, indicating that these protons were encapsulated into the cavity of CB[8]. Moreover, the proton of triazole (H_g) shifted downfield to 8.13 ppm ($\Delta\delta = 0.20$ ppm), which might result from the hydrogen–bonding interactions with the carbonyl groups in CB[8], indicating that the triazole group was located outside the cavity of CB[8]. The chemical shifts of these protons were no longer changed when the amount of CB[8] increased above 0.5 eq., presenting a slow exchange within the NMR timescale. Moreover, 2D ROESY spectroscopy was carried out to confirm the binding model. As shown in Fig. S4 (SI), strong NOE correlation peaks could be observed between $H_{c'}$ and $H_{a'}$, while no NOE correlation peaks could be observed between un-encapsulated H_c and H_a. These results indicated the head-to-tail stacking model of the BQ motif in the CB[8] cavity. Meanwhile, diffusion ordered spectroscopy (DOSY) was also employed. As shown in the recorded spectra (Fig. S5 and S6, SI), the diffusion coefficients of BQ-PCD and BQ-PCD⊂CB[8] were determined to be 1.99×10^{-10} m^2 s^{-1} and 1.41×10^{-10} m^2 s^{-1}, respectively. The decrease in diffusion coefficient indicated the formation of a host–guest complex in the presence of CB[8].

Then, UV-vis spectroscopy was employed to study the host–guest binding behaviour with CB[8]. From the Job plot of the BQ-PCD and CB[8] complex (Fig. S7, SI), the inflection point was observed at a molar ratio of 0.67 ([BQ-PCD]/([BQ-PCD] + [CB[8]]), indicating the 1 : 2 stoichiometry binding behaviour between CB[8] and BQ-PCD (Fig. 1b). Furthermore, as shown in Fig. S8 (SI), the peaks at 1194.5026 (*m*/*z*, [2BQ-PCD + CB[8]-2Br + 2Na]$^{4+}$) could be observed, which confirmed the 2 : 1 host–guest complex between BQ-PCD and CB[8]. Then, the binding constant was further determined by a UV-vis titration experiment. From the obtained UV-vis titration spectra between BQ-PCD and CB[8] (Fig. S9, SI), the characteristic absorption peak of BQ-PCD at 243 nm gradually decreased with the addition of CB[8], and equilibrium was reached upon the addition of 0.8 eq. of CB[8]. Moreover, the BQ-PCD⊂CB[8] complex exhibited an increased absorbance band in the range from 340 to 361 nm with the iso-absorptive point at 341 nm (Fig. S10, SI). This result indicated that intermolecular charge transfer would occur in the presence of CB[8], which might result from the π–π stacking of two 6-bromoisoquinolium motifs in the cavity of CB[8], and might facilitate multi-photon absorption. And nonlinear curve fitting was employed to determine the binding constants, whose values were $K_1 = (1.21 \pm 0.18) \times 10^5$ M^{-1} and $K_2 = (1.73 \pm 0.97) \times 10^5$ M^{-1} (Fig. 1e). The Hill equation was also employed to quantitatively evaluate the molecular recognition behavior between BQ-PCD and CB[8] (Fig. S11, SI). The log *K* values in CB[8] complexes were determined to be (9.87 ± 0.24), respectively, and the Hill coefficient was determined to be 1.83, indicating the 2 : 1 stoichiometry for BQ-PCD⊂CB[8], which were well

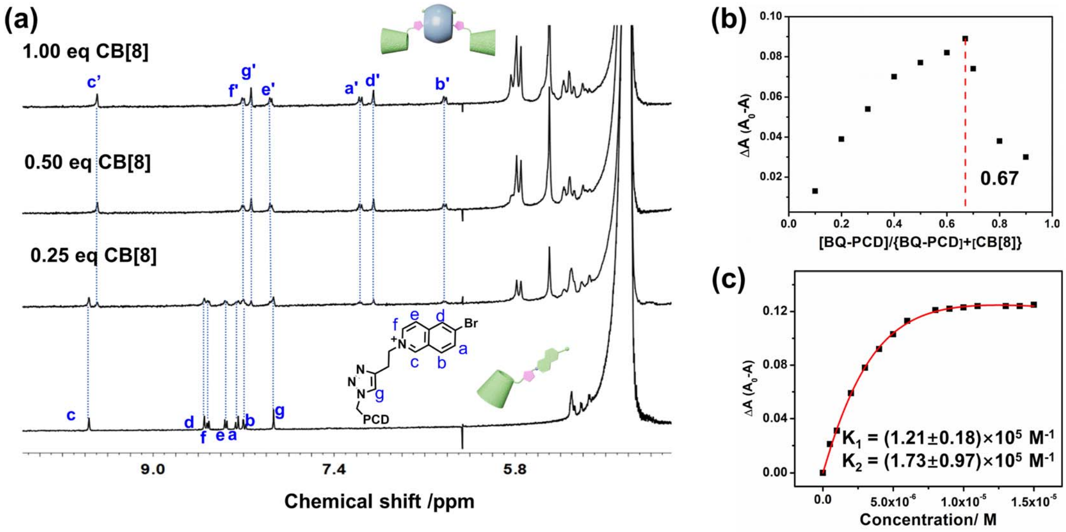

Fig. 1 (a) Partial ^{1}H NMR (400 MHz, D_2O, 298 K) spectra of BQ-PCD and CB[8] ([BQ-PCD] = 1 mM, [CB[8]] = 0–1 mM), (b) Job plot showing 2 : 1 stoichiometry between BQ-PCD and CB[8] ([BQ-PCD] + [CB[8]] = 10 μM), (c) nonlinear curve fitting of absorption intensity change at 243 nm of BQ-PCD *versus* varying concentrations of CB[8] ([BQ-PCD] = 10 μM, [CB[8]] = 0–15 μM).

consistent with the above results. Overall, the above results indicated the strong binding behavior between BQ-PCD and CB[8] could be successfully achieved.

Photophysical properties of BQ-PCD⊂CB[8]

After verifying the binding behavior between BQ-PCD and CB[8], the luminescent behavior of BQ-PCD⊂CB[8] in an aqueous solution was investigated. Initially, the photoluminescence spectra of the BQ-PCD exhibited two emission peaks at 377 nm and 530 nm (Fig. 2a), giving an average lifetime of 6.7 ns at 377 nm and 13.8 ns at 530 nm (Fig. S12, SI). Upon the gradual addition of CB[8] into the BQ-PCD solution, the emission peak at 377 nm gradually decreased, and the emission peak at 530 nm increased, and stabilized when the CB[8] concentration reached 0.8 equivalent (Fig. 2a). Additionally, in the delayed spectra (delay time = 0.05 ms), only the emission at 530 nm gradually increased upon the addition of CB[8] to the BQ-PCD solution (Fig. 2b), indicating that the emission at 530 nm exhibited a long-lived feature. Moreover, the emission at 530 nm exhibited a significant overlap with the normalized gated emission spectrum and the photoluminescence spectrum (Fig. 2b inset), indicating the long-lived emission with the addition of CB[8]. Through lifetime decay testing, the lifetime at 377 nm of BQ-PCD⊂CB[8] was determined to be 4.3 ns (Fig. S13, SI), and the lifetime at 530 nm increased to 640.0 μs (Fig. 2c), suggesting that the emission at 530 nm belonged to long-lived phosphorescence. And the phosphorescence QY of BQ-PCD⊂CB[8] was determined to be 2.4% (Fig. S14, SI).

Subsequently, with bubbling N_2 into BQ-PCD⊂CB[8] solution, the emission intensity at 530 nm significantly enhanced (Fig. 2d), which was attributed to the suppression of the triplet electron quenching by oxygen, confirming the phosphorescence nature of emission at 530 nm in solution. Moreover, it could be observed that with the decrease of the temperature from 330 K to 77 K, the long-lived emission intensity at 530 nm was steadily enhanced (Fig. S15, SI), which provided a solid confirmation of the phosphorescence characteristic in the BQ-PCD⊂CB[8] complex. The temperature-dependent decay curve was also recorded, and the lifetime of BQ-PCD⊂CB[8] at 530 nm was remarkably prolonged from 640.0 μs to 8.6 ms at 77 K (Fig. S16, SI). The amalgamation of these experimental results collectively substantiated that both the enhanced phosphorescence QY and prolonged phosphorescent emission life-time would be achieved taking advantage of the macrocyclic confinement effect of CB[8] encapsulating 6-bromoisoquinolium into its cavities.

In the above study, it was demonstrated that BQ units adopted a head-to-tail stacking model in the BQ-PCD⊂CB[8] complex, which could enhance the π–π stacking interaction and improve the intermolecular charge transfer ability, which possibly facilitated the multi-photon absorption ability. Then, the upconversion property of the BQ-PCD⊂CB[8] complex was investigated. The multi-photon absorption scan of the BQ-PCD⊂CB[8] complex was performed over the excitation wavelength range of 700–1100 nm and a clear three-photon absorption peak was observed at 920 nm (Fig. 2e). Under 920 nm excitation, the BQ-PCD⊂CB[8] complex exhibited an emission peak around 530 nm (Fig. 2f), which overlaps well with the spectrum collected under one-photon excitation at 300 nm, further confirming its multi-photon absorption behaviour. Thus, the BQ-PCD⊂CB[8] complex featured delayed emission properties under NIR excitation, making it an ideal candidate for bioimaging due to the reduced photodamage and background fluorescence, as well as its deep tissue penetration ability under NIR excitation.

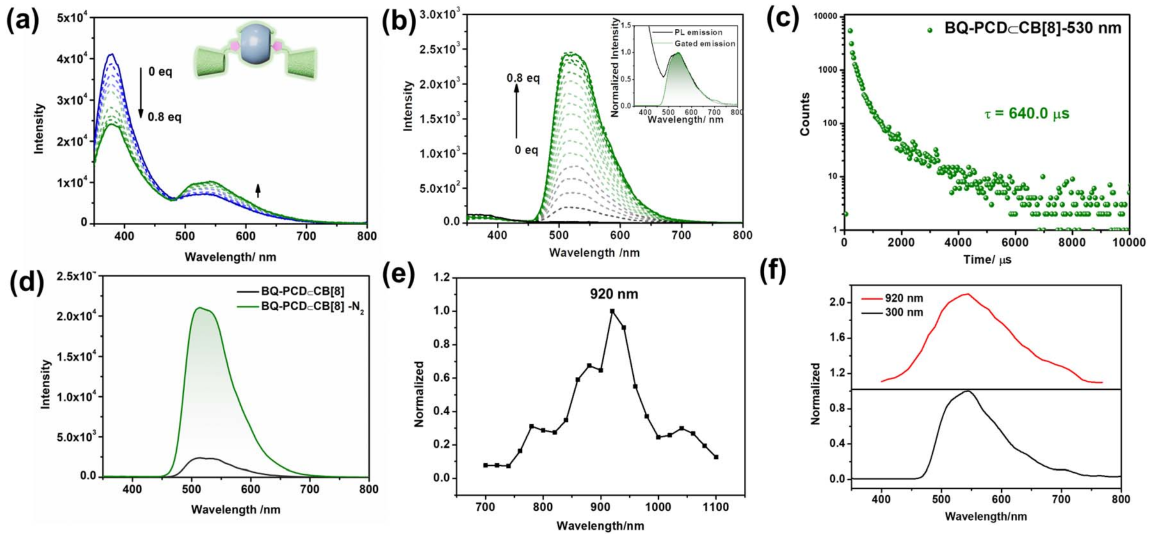

Fig. 2 (a) Photoluminescence spectra of BQ-PCD upon adding CB[8] ([BQ-PCD] = 10 μM, [CB[8]] = 0–8 μM), (b) gated emission spectra (delay time = 0.05 ms) of BQ-PCD upon adding CB[8] ([BQ-PCD] = 10 μM, [CB[8]] = 0–8 μM, λ_{ex} = 300 nm), (inset) normalized photoluminescence and gated emission spectra (delay time = 0.05 ms) of BQ-PCD⊂CB[8], (c) time-resolved photoluminescence decay spectrum of BQ-PCD⊂CB[8] at 530 nm, (d) gated emission spectra of BQ-PCD⊂CB[8] with pumping N_2 (delay time = 0.05 ms, [BQ-PCD] = 10 μM, [CB[8]] = 5 μM, λex = 300 nm), (e) two-photon absorption spectrum of BQ-PCD⊂CB[8] in water ([BQ-PCD] = 10 μM, [CB[8]] = 5 μM), (f) emission spectra of BQ-PCD⊂CB[8] excited at 300 (black curve) and 920 nm (red curve) ([BQ-PCD] = 10 μM, [CB[8]] = 5 μM).

Host–guest properties between BQ-PCD$\subset$CB[8] and TPPS

Long-lifetime emissive materials with large Stokes shifts are emerging as promising candidates in the field of optical materials, and such properties can be achieved through the phosphorescence resonance energy transfer (PRET) process, in which the energy of the phosphorescence donor would transfer to a fluorescent acceptor, leading to delayed fluorescence with a large red shift. Efficient PRET requires not only an excellent overlap between the emission spectrum of the donor and the excitation spectrum of the acceptor, but also a close spatial distance between them. TPPS is selected as the fluorescent acceptor, as it exhibits the distinctive absorption peaks of the Soret band at 411 nm and the Q-band between 450 and 700 nm, and the absorption peak of the Q-band overlapped well with the phosphorescence emission spectrum of BQ-PCD$\subset$CB[8] (Fig. 3a). Meanwhile, permethylated β-cyclodextrin (PCD) binds TPPS in aqueous solution with strong affinity, thereby reducing the spatial distance between the phosphorescent donor BQ-PCD$\subset$CB[8] and the acceptor TPPS. Therefore, the occurrence of efficient PRET can be anticipated due to the effective spectral overlap and the reduced spatial distance between the donor and acceptor.

The previous studies demonstrated that the PCD moiety in BQ-PCD can encapsulate TPPS with a 2 : 1 stoichiometry.[35] From the UV-vis titration, upon addition of BQ-PCD into TPPS, the Soret band at 414 nm and the Q-band between 450 and 700 nm both increased (Fig. S17, SI), indicating the encapsulation of TPPS into the cavity of BQ-PCD. To confirm the occurrence of dual host–guest interaction in the TPPS$\subset$BQ-PCD$\subset$CB[8] complex, ^{1}H NMR spectroscopy was employed. As depicted in Fig. S18 (SI), upon the addition of BQ-PCD, the protons of TPPS split into two sets, indicating the successful formation of the host–guest complex between PCD and TPPS. And following addition of CB[8], the protons of the BQ motif in the ternary system exhibited obvious upfield shifts, similarly to the BQ-PCD$\subset$CB[8] complex. Meanwhile, the protons of TPPS exhibited little change compared with TPPS$\subset$BQ-PCD, indicating the simultaneous existence of dual host–guest complexation behavior in TPPS$\subset$BQ-PCD$\subset$CB[8]. These results indicated the ternary host–guest complexation could be successfully constructed.

PRET process between BQ-PCD$\subset$CB[8] and TPPS

Due to the excellent overlap between the phosphorescence emission of BQ-PCD$\subset$CB[8] at 530 nm and the Q-band of TPPS, efficient PORTP energy transfer was proposed through the closer spatial distance within the ternary host–guest complex of TPPS$\subset$BQ-PCD$\subset$CB[8]. The PRET process was investigated under excitation at 300 nm. As shown in Fig. 3b, when TPPS was added into BQ-PCD$\subset$CB[8] solution, the phosphorescent emission at 530 nm gradually diminished, and simultaneously emerging emission peaks at 645 nm and 710 nm appeared in the gated emission spectra (delay time = 0.05 ms). The time-gated emission peaks at 645 nm and 710 nm were consistent with the characteristic fluorescence emission peaks of free TPPS, indicating the successful PRET from phosphor BQ-PCD to TPPS for long-lived deep-red fluorescence emission. Upon addition of 0.5 eq. of TPPS into BQ-PCD$\subset$CB[8] solution, the phosphorescence emission at 530 nm nearly disappeared, indicating a high energy transfer efficiency to TPPS. The time-resolved decay curves revealed that the phosphorescence lifetime at 530 nm decreased from 640.0 μs to 35.1 μs in TPPS$\subset$BQ-

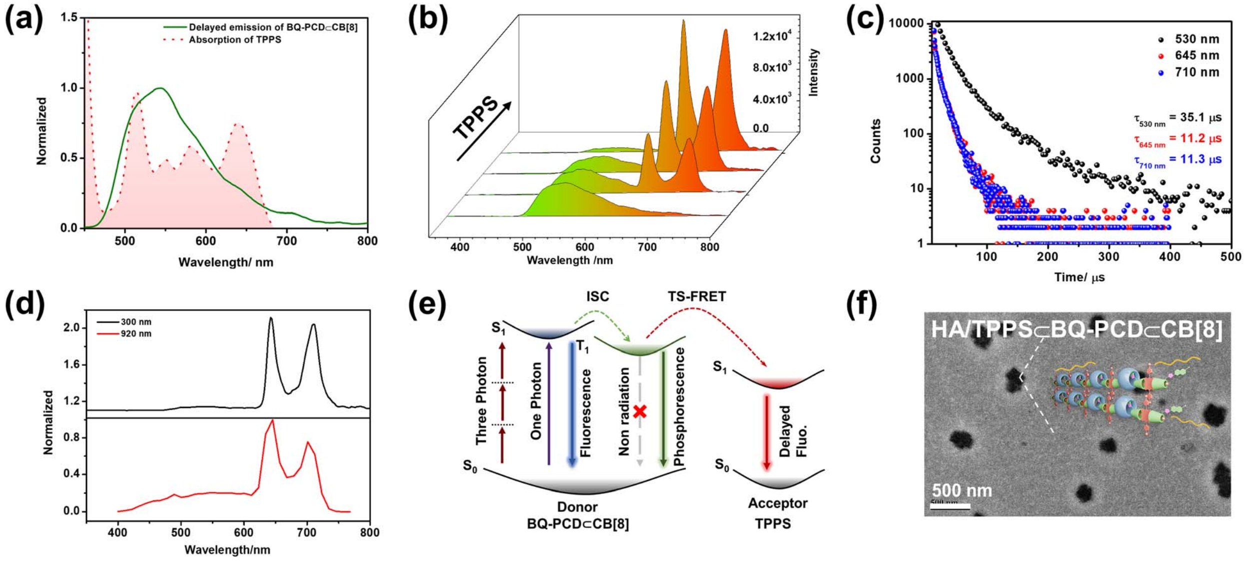

Fig. 3 (a) Normalized phosphorescence emission spectra of BQ-PCD$\subset$CB[8], and normalized absorption spectra of TPPS, (b) phosphorescence emission spectra of BQ-PCD$\subset$CB[8] in the presence of various concentrations of TPPS (delay time = 0.05 ms, [BQ-PCD] = 10 μM, [CB[8]] = 5 μM, [TPPS] = 0–6 μM, λ_{ex} = 300 nm), (c) time-resolved photoluminescence decay spectra of TPPS$\subset$BQ-PCD$\subset$CB[8] at 530 nm, 645 nm, and 710 nm, (d) diagram of the possible mechanism for the RTP energy transfer process (ISC = intersystem crossing, TS-FRET = triplet-to-singlet Förster resonance energy transfer), (e) emission spectra of TPPS$\subset$BQ-PCD$\subset$CB[8] excited at 300 (black curve) and 920 nm (red curve) ([BQ-PCD] = 10 μM, [CB[8]] = 5 μM, [TPPS] = 5 μM), (f) TEM image of HA/TPPS$\subset$BQ-PCD$\subset$CB[8].

PCD⊂CB[8] assemblies (Fig. 3c). In addition, the lifetime at 645 nm and 710 nm was determined to be 11.2 μs and 11.3 μs in TPPS⊂BQ-PCD⊂CB[8] assemblies, both of which exhibited the long-lived features in the microsecond range. The energy transfer efficiency (Φ_{PRET}) was further calculated by the lifetime changes of donor complexes, giving a Φ_{PRET} value of 94.5% from BQ-PCD⊂CB[8] to TPPS. Meanwhile, the delayed fluorescence quantum yield (QY) of TPPS⊂BQ-PCD⊂CB[8] (Fig. S19, SI) was determined to be 3.9%. Moreover, the bubbling of N$_2$ into the TPPS⊂BQ-PCD⊂CB[8] solution could lead to the enhancement in the emission intensity at 530 nm, 645 nm, and 710 nm (Fig. S20, SI), which could suppress the oxygen-mediated triplet electron quenching process for better RTP performance, further confirming the PRET process. The lifetimes were measured after the bubbling of N$_2$ (Fig. S21 and S22, SI), and the lifetimes of 645 nm and 710 nm further increased to 18.2 μs and 17.3 μs in TPPS⊂BQ-PCD⊂CB[8], indicating that the long-lived emission was sensitive to the resolved oxygen in aqueous solution. These phenomena demonstrated the effective phosphorescent energy transfer process from the triplet state of BQ-PCD⊂CB[8] to the singlet state of TPPS, leading to the long-lived deep-red luminescence.

To further confirm the macrocycle-mediated efficient energy transfer process, a series of control experiments were also conducted. Firstly, in the time-gated luminescence spectra of TPPS⊂BQ-PCD (Fig. S23, SI), almost no delayed emission could be detected under excitation at 300 nm. And with the addition of CB[8] into TPPS⊂BQ-PCD solution, delayed fluorescence at 645 nm and 710 nm emerged (Fig. S24, SI), indicating that the delayed deep-red fluorescence of TPPS originated from the phosphorescence emission induced by the CB[8] confinement effect. Furthermore, by investigating the excitation wavelength selectivity, we found that at an excitation wavelength of 414 nm, no significant enhancement in the emission at 645 nm and 710 nm could be observed in the time-gated luminescence spectra of TPPS⊂BQ-PCD⊂CB[8] (Fig. S25, SI). According to the time-resolved decay curves, under 450 nm excitation, the lifetimes of TPPS⊂BQ-PCD⊂CB[8] were measured to be 13.1 ns (645 nm) and 12.7 ns (710 nm) (Fig. S26, SI), respectively. Therefore, the TPPS⊂BQ-PCD⊂CB[8] exhibited no long-lived emission properties under 414 nm excitation. Therefore, through the dual macrocyclic confinement effect from CB[8] and PCD, an efficient phosphorescent energy transfer system could be successfully achieved for the well-overlap in the phosphorescence emission spectrum and absorbance spectrum of TPPS, as well as the closer distance between the phosphor donor and TPPS, leading to a long-lived deep-red fluorescence system with high PRET efficiency.

Transmission electron microscopy (TEM) was employed to investigate the assembly morphologies. Interestingly, the stoichiometric ratio between BQ-PCD and CB[8] was determined to be 2 : 1, along with the 2 : 1 binding stoichiometric ratio of BQ-PCD and TPPS, which would result in the formation of a supramolecular polymer in TPPS⊂BQ-PCD⊂CB[8], further self-assembled into nanofibers (Fig. S27, SI).

Subsequently, the upconversion properties of the ternary host–guest complex (TPPS⊂BQ-PCD⊂CB[8]) were investigated. Under 920 nm excitation, the emission spectrum of TPPS⊂BQ-PCD⊂CB[8] showed a pronounced decrease in the 530 nm emission peak compared to BQ-PCD⊂CB[8], along with the emergence of characteristic emission peaks at 645 nm and 710 nm (Fig. 3d), confirming that long-lived deep-red PRET fluorescence could also be successfully achieved under three-photon excitation (Fig. 3e). Therefore, the TPPS⊂BQ-PCD⊂CB[8] supramolecular assemblies with long-lived deep-red luminescence encouraged us to investigate their potential application in bioimaging.

Upconversion-mediated cell imaging

Hyaluronic acid (HA), which possesses excellent water solubility, biocompatibility, and biodegradability, and can be specifically recognized by CD44 receptor protein overexpressed on tumor cell surface,[36,37] was introduced for cascade assembly through multivalent interactions, anticipating to achieve cancer cell-targeting delayed deep-red fluorescence imaging. After addition of HA into the TPPS⊂BQ-PCD⊂CB[8] assembly, the TEM images of HA/TPPS⊂BQ-PCD⊂CB[8] showed nanoparticles with a diameter of around 300 nm (Fig. 3f). Firstly, its biocompatibility was evaluated on the HeLa cell line by CCK-8 assay, in which the high survival rates suggested that the HA/TPPS⊂BQ-PCD⊂CB[8] assemblies exhibited negligible toxicity to HeLa cells (Fig. S22, SI), making it an ideal candidate for bioimaging. After being incubated with HA/TPPS⊂BQ-PCD⊂CB[8] assemblies for 12 h, the bright red signal could be observed in the cytoplasm of HeLa cells (Fig. 4a), which resulted from the PRET-based long-lived deep-red fluorescence. Furthermore, from the obtained CLSM images of HeLa cells treated with TPPS and TPPS⊂BQ-PCD⊂CB[8] (Fig. S29 and S30, SI), relatively weaker fluorescence in the HeLa cells could be observed compared with the HA/TPPS⊂BQ-PCD⊂CB[8] group, confirming the introduction of HA would lead to high uptake efficiency into cancer cells. Moreover, cellular imaging was also conducted in the L929 normal cells line, and a weak red signal was detected, indicative of the poor uptake efficiency into the normal cells (Fig. S31, SI). These results jointly confirmed the cellular uptake behavior might result from the specific recognition between HA and its CD44 acceptor overexpressed on HeLa cells. This also indicated that the HA/TPPS⊂BQ-PCD⊂CB[8] assemblies can be successfully utilized for cancer cell-targeted fluorescence imaging.

Furthermore, the cell imaging behaviour of the assemblies was also investigated under irradiation at 920 nm to confirm its multi-photon absorption property *in vitro*. From the multi-photon fluorescence microscopy images of BQ-PCD⊂CB[8], the green fluorescence could be observed (Fig. 4b), indicating the multi-photon absorption ability was retained in the cellular environment. Compared with the fluorescence images of free BQ-PCD and BQ-PCD⊂CB[7]35 (Fig. S32, SI), the fluorescence intensity significantly increased in BQ-PCD⊂CB[8], which confirmed the confinement effect of CB[8] could remarkably enhance the multi-photon absorption ability due to the existence of strong intermolecular charge transfer ability in the host–guest complex. Meanwhile, the multi-photon imaging

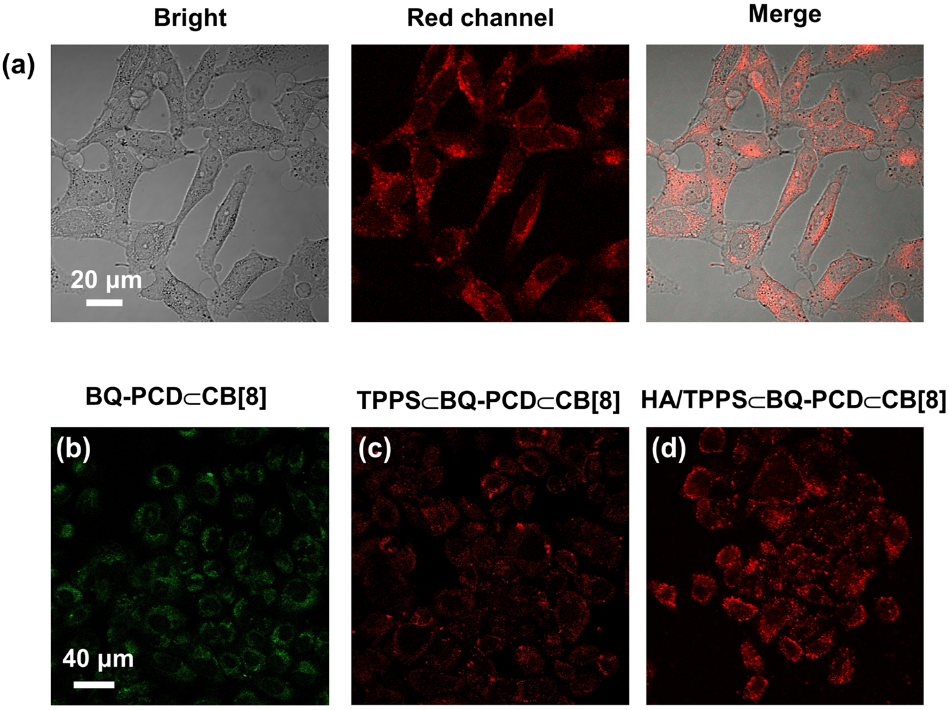

Fig. 4 (a) One-photon CLSM images of HeLa cells incubated with HA/TPPS⊂BQ-PCD⊂CB[8] ([BQ-PCD] = 10 μM, [CB[8]] = 5 μM, [TPPS] = 5 μM, [HA] = 20 μg mL^{-1}), three-photon CLSM images of HeLa cells incubated with (b) BQ-PCD⊂CB[8] (emission was collected at 500–580 nm, [BQ-PCD] = 10 μM, [CB[8]] = 5 μM), (c) TPPS⊂BQ-PCD⊂CB[8] (emission was collected at 620–740 nm, [BQ-PCD] = 10 μM, [CB[8]] = 5 μM, [TPPS] = 5 μM), (d) HA/TPPS⊂BQ-PCD⊂CB[8] (emission was collected at 620–740 nm, [BQ-PCD] = 10 μM, [CB[8]] = 5 μM, [TPPS] = 5 μM, [HA] = 20 μg mL^{-1}).

ability of TPPS was also investigated, which provided very weak red fluorescence in cells (HeLa cell line) under excitation at 920 nm (Fig. S33, SI). Interestingly, brighter red fluorescence could be observed in the TPPS⊂BQ-PCD⊂CB[8] group (Fig. 4c), indicating deep-red fluorescence resulted from the PRET process in this ternary complex. We further employed the normal cells (L929 cells) to investigate the function of HA in the three-photon absorption properties, which could dismiss the HA-enhanced uptake behaviour in cells. From the obtained upconversion CLSM images (Fig. S34, SI), it could be found that the three-photon emission signal of BQ-PCD⊂CB[8] is almost unaffected in the presence of HA. Finally, the HA-enhanced cellular uptake efficiency could also be deduced from the multi-photon fluorescence images, in which brighter red fluorescence would be observed compared with the TPPS⊂BQ-PCD⊂CB[8] group (Fig. 4d). These phenomena were similar to the one-photon fluorescence imaging. All these results collectively confirm the multi-photon absorption mediated PRET process could be achieved *in vitro*, making it an ideal candidate for bioimaging.

Conclusions

In summary, we reported a cascade assembly with an upconversion PRET process, in which CB[8] could encapsulate the upconversion phosphor guest (BQ-PCD) for enhanced PORTP at 530 nm. Meanwhile, due to the macrocyclic confinement-enhanced multi-photon absorption ability, the PORTP could also be achieved under excitation at 920 nm in BQ-PCD⊂CB[8]. Moreover, the cascade complexation with TPPS would result in delayed deep-red fluorescence with a highly efficient PRET process through strong host–guest interaction, which could be realized under irradiation at both 300 nm and 920 nm. This upconversion-based PRET process made this delayed deep-red fluorescence assembly an ideal candidate for bioimaging. After the co-assembly with the tumour-targeting agent (HA), the supramolecular cascade assembly (HA/TPPS⊂BQ-PCD⊂CB[8]) also exhibited an efficient upconversion PRET process, in which the delayed deep-red fluorescence could also be achieved under excitation at 920 nm, successfully being applied for targeted cancer cell imaging. This macrocyclic confinement assembly which improved both the PORTP and upconversion abilities of phosphors would provide a convenient way to construct delayed fluorescence materials under NIR excitation, which would further expand their potential application in bioimaging or biosensing due to its deep tissue penetration ability and high signal to noise ratio.

Author contributions

The manuscript was written through contributions of all authors. Conceptualization: JN, XW, YL; methodology: JN, XW, JY, LHW; investigation: JN, JY, XW, ZL, JW; visualization: JN, JY, XW; supervision: YMZ, JH, YL; writing—original draft: JN, XW; writing—review & editing: JN, XW, YMZ, YL.

Conflicts of interest

There are no conflicts to declare.

Data availability

The data supporting this article have been included as part of the SI. Supplementary information: Details of the characterization of target compounds, NMR data; UV-Vis absorbance spectra; photoluminescence/delayed spectra, and time-resolved spectra; TEM images; CCK8 results and CLSM images. See DOI: https://doi.org/10.1039/d5sc05297a.

Acknowledgements

This work was financially supported by the National Natural Science Foundation of China (22171148, 22371148, 22131008, 22101280, and 22201142), the Natural Science Foundation of Tianjin (21JCZDJC00310), Haihe Laboratory of Sustainable Chemical Transformation, and the Fundamental Research Funds for the Central Universities (Nankai University).

Notes and references

1 X. Dou, X. Wang, X. Xie, J. Zhang, Y. Li and B. Tang, Advances in polymer-based organic room-temperature phosphorescence materials, *Adv. Funct. Mater.*, 2024, **34**, 2314069.

2 H. Sun and L. Zhu, Achieving purely organic room temperature phosphorescence in aqueous solution, *Aggregate*, 2023, **4**, e253.

3 Z.-Y. Zhang and Y. Liu, Ultralong room-temperature phosphorescence of a solid-state supramolecule between phenylmethylpyridinium and cucurbit[6]uril, *Chem. Sci.*, 2019, **10**, 7773–7778.

4 S. Garain, A. A. Kongasseri, S. M. Wagalgave, R. Konar, D. Deb, K. S. Narayan, P. K. Samanta and S. J. George, Supramolecular charge-transfer approach for tunable and efficient circularly polarized delayed fluorescence and phosphorescence, *Angew. Chem., Int. Ed.*, 2025, **64**, e202501330.

5 Y. Zhang, J. Li, J. Zhao, X. Li, Z. Wang, Y. Huang, H. Zhang, Q. Liu, Y. Lei and D. Ding, π–π interaction-induced organic long-wavelength room-temperature phosphorescence for *in vivo* atherosclerotic plaque imaging, *Angew. Chem., Int. Ed.*, 2024, **63**, e202313890.

6 Y. Fan, S. Liu, M. Wu, L. Xiao, Y. Fan, M. Han, K. Chang, Y. Zhang, X. Zhen, Q. Li and Z. Li, Mobile phone flashlight-excited red afterglow bioimaging, *Adv. Mater.*, 2022, **34**, 2201280.

7 Y. Peng, X. Yao, X. Hu, B. Wu, X. Pei, Y. Yang, Z. Dong, Z. An, W. Huang and T. Cai, Edible ultralong organic phosphorescent excipient for afterglow visualizing the quality of tablets, *Adv. Mater.*, 2024, **36**, 2406618.

8 Z. Yang, J. Qian, S. Zhao, Y. Lv, Z. Feng, S. Wang, H. He, S.-T. Zhang, H. Liu and B. Yang, Highly sensitive thianthrene covalent trimer room-temperature phosphorescent materials for low-concentration oxygen detection, *Angew. Chem., Int. Ed.*, 2025, **64**, e202424669.

9 M. Cao, Y. Ren, Y. Wu, J. Shen, S. Li, Z.-Q. Yu, S. Liu, J. Li, O. J. Rojas and Z. Chen, Biobased and biodegradable films exhibiting circularly polarized room temperature phosphorescence, *Nat. Commun.*, 2024, **15**, 2375.

10 J. Lu, Y. Niu, C. Jin, C. Wu, H. Wang, Y. Guan, P. Wang and X. Fan, Time-dependent color-tunable room temperature phosphorescence from unusual conformational transitions in phenothiazine polymers under UV irradiation, *Sci. China Chem.*, 2025, **68**, 1091–1098.

11 X. Nie, J. Gong, Z. Ding, B. Wu, W.-J. Wang, F. Gao, G. Zhang, P. Alam, Y. Xiong, Z. Zhao, Z. Qiu and B. Z. Tang, Room temperature phosphorescent nanofiber membranes by bio-fermentation, *Adv. Sci.*, 2024, **11**, 2405327.

12 P. Samadder, K. Naim, S. C. Sahoo and P. P. Neelakandan, Surface coating induced room-temperature phosphorescence in flexible organic single crystals, *Chem. Sci.*, 2024, **15**, 9258–9265.

13 H. Shi, W. Yao, W. Ye, H. Ma, W. Huang and Z. An, Ultralong organic phosphorescence: from material design to applications, *Acc. Chem. Res.*, 2022, **55**, 3445–3459.

14 S. M. Wagalgave, A. A. Kongasseri, U. Singh, A. Anilkumar, S. N. Ansari, S. K. Pati and S. J. George, Core-substituted pyromellitic diimides: a versatile molecular scaffold for tunable triplet emission, *J. Am. Chem. Soc.*, 2025, **147**, 15591–15601.

15 B. Chang, J. Chen, J. Bao, T. Sun and Z. Cheng, Molecularly engineered room-temperature phosphorescence for biomedical application: from the visible toward second near-infrared window, *Chem. Rev.*, 2023, **123**, 13966–14037.

16 J. Gu, W. Yuan, K. Chang, C. Zhong, Y. Yuan, J. Li, Y. Zhang, T. Deng, Y. Fan, L. Yuan, S. Liu, Y. Xu, S. Ling, C. Li, Z. Zhao, Q. Li, Z. Li and B. Z. Tang, Organic materials with ultrabright phosphorescence at room temperature under physiological conditions for bioimaging, *Angew. Chem., Int. Ed.*, 2025, **64**, e202415637.

17 Y. Li, Z. Wu, Z. Huang, C. Yin, H. Tian and X. Ma, Activatable red/near-infrared aqueous organic phosphorescence probes for improved time-resolved bioimaging, *Nat. Sci. Rev.*, 2024, **12**, nwae383.

18 Y. Zhao, J. Yang, C. Liang, Z. Wang, Y. Zhang, G. Li, J. Qu, X. Wang, Y. Zhang, P. Sun, J. Shi, B. Tong, H.-Y. Xie, Z. Cai and Y. Dong, Fused-ring pyrrole-based near-infrared emissive organic RTP material for persistent afterglow bioimaging, *Angew. Chem., Int. Ed.*, 2024, **63**, e202317431.

19 X. Wu, T.-L. Zhuang, M. Liu, X. Sun, L. Zhu, Q. Zhang, J. Han, L. Wang and R. Guo, In situ supramolecular self-assembly of a perylene diimide derivative in mitochondria for cancer cell ferroptosis, *Org. Chem. Front.*, 2024, **11**, 6055–6063.

20 X. Yang, G. I. N. Waterhouse, S. Lu and J. Yu, Recent advances in the design of afterglow materials: mechanisms, structural regulation strategies and applications, *Chem. Soc. Rev.*, 2023, **52**, 8005–8058.

21 W. Zhao, Z. He and B. Z. Tang, Room-temperature phosphorescence from organic aggregates, *Nat. Rev. Mater.*, 2020, **5**, 869–885.

22 M. Yang, H. Gong, D. Yang, L. Feng, S. Gai, F. Zhang, H. Ding, F. He and P. Yang, Research progress on rare earth up-conversion and near-infrared II luminescence in biological applications, *Chin. Chem. Lett.*, 2024, **35**, 108468.

23 T. T. Tran, B. Regan, E. A. Ekimov, Z. Mu, Y. Zhou, W.-b. Gao, P. Narang, A. S. Solntsev, M. Toth, I. Aharonovich and C. Bradac, Anti-Stokes excitation of solid-state quantum emitters for nanoscale thermometry, *Sci. Adv.*, 2019, **5**, eaav9180.

24 Y. Zheng, H. Wei, P. Liang, X. Xu, X. Zhang, H. Li, C. Zhang, C. Hu, X. Zhang, B. Lei, W.-Y. Wong, Y. Liu and J. Zhuang, Near-infrared-excited multicolor afterglow in carbon dots-based room-temperature afterglow materials, *Angew. Chem., Int. Ed.*, 2021, **60**, 22253–22259.

25 W.-L. Zhou, Y. Chen, Q. Yu, H. Zhang, Z.-X. Liu, X.-Y. Dai, J.-J. Li and Y. Liu, Ultralong purely organic aqueous phosphorescence supramolecular polymer for targeted tumor cell imaging, *Nat. Commun.*, 2020, **11**, 4655.

26 P. Wei, X. Zhang, J. Liu, G.-G. Shan, H. Zhang, J. Qi, W. Zhao, H. H. Y. Sung, I. D. Williams, J. W. Y. Lam and B. Z. Tang, New wine in old bottles: prolonging room-temperature phosphorescence of crown ethers by supramolecular interactions, *Angew. Chem., Int. Ed.*, 2020, **59**, 9293–9298.

27 S. J. Barrow, S. Kasera, M. J. Rowland, J. del Barrio and O. A. Scherman, Cucurbituril-based molecular recognition, *Chem. Rev.*, 2015, **115**, 12320–12406.

28 G. Wu, F. Li, B. Tang and X. Zhang, Molecular engineering of noncovalent dimerization, *J. Am. Chem. Soc.*, 2022, **144**, 14962–14975.

29 J. Wang, Z. Huang, X. Ma and H. Tian, Visible-light-excited room-temperature phosphorescence in water by cucurbit[8]uril-mediated supramolecular assembly, *Angew. Chem., Int. Ed.*, 2020, **59**, 9928–9933.

30 J. Yu, J. Niu, H. Wang, C.-H. Wang and Y. Liu, Supramolecular two-photon switch for near-infrared (NIR) cell imaging, *Adv. Opt. Mater.*, 2024, **12**, 2301473.

31 F.-F. Shen, Y. Chen, X. Dai, H.-Y. Zhang, B. Zhang, Y. Liu and Y. Liu, Purely organic light-harvesting phosphorescence energy transfer by β-cyclodextrin pseudorotaxane for mitochondria targeted imaging, *Chem. Sci.*, 2021, **12**, 1851–1857.

32 W.-L. Zhou, W. Lin, Y. Chen and Y. Liu, Supramolecular assembly confined purely organic room temperature phosphorescence and its biological imaging, *Chem. Sci.*, 2022, **13**, 7976–7989.

33 X.-Y. Dai, M. Huo and Y. Liu, Phosphorescence resonance energy transfer from purely organic supramolecular assembly, *Nat. Rev. Chem.*, 2023, **7**, 854–874.

34 S. Garain, B. C. Garain, M. Eswaramoorthy, S. K. Pati and S. J. George, Light-harvesting supramolecular phosphors: highly efficient room temperature phosphorescence in solution and hydrogels, *Angew. Chem., Int. Ed.*, 2021, **60**, 19720–19724.

35 J. Niu, X. Wu, J. Yu, Z. Lei, Y.-M. Zhang, L.-H. Wang and Y. Liu, Cucurbit[7]uril-confined cascade assembly of cyclodextrin phosphor derivative achieving multicolor delayed luminescence for information encryption, *Chin. Chem. Lett.*, 2025, DOI: **10.1016/j.cclet.2025.111419**.

36 S.-Y. Han, H. S. Han, S. C. Lee, Y. M. Kang, I.-S. Kim and J. H. Park, Mineralized hyaluronic acid nanoparticles as a robust drug carrier, *J. Mater. Chem.*, 2011, **21**, 7996–8001.

37 Z. Liu, W. Lin and Y. Liu, Macrocyclic supramolecular assemblies based on hyaluronic ccid and their biological applications, *Acc. Chem. Res.*, 2022, **55**, 3417–3429.